

## The shocking features in the closest rich galaxy cluster Norma

CHONG GE <sup>1</sup>, MING SUN <sup>2</sup>, MPATI RAMATSOKU <sup>3,4</sup>, CHRIS NOLTING <sup>5</sup> AND BÄRBEL S. KORIBALSKI <sup>6,7</sup>

<sup>1</sup>*Department of Astronomy, Xiamen University, Xiamen, Fujian 361005, China*

<sup>2</sup>*Department of Physics & Astronomy, University of Alabama in Huntsville, 301 Sparkman Dr NW, Huntsville, AL 35899, USA*

<sup>3</sup>*Centre for Radio Astronomy Techniques and Technologies (RATT), Department of Physics and Electronics, Rhodes University, Makhanda, 6140, South Africa*

<sup>4</sup>*INAF-Osservatorio Astronomico di Cagliari, Via della Scienza 5, I-09047 Selargius (CA), Italy*

<sup>5</sup>*Gustavus Adolphus College, Saint Peter, Minnesota, USA*

<sup>6</sup>*Australia Telescope National Facility, CSIRO, Space and Astronomy, P.O. Box 76, Epping, NSW 1710, Australia*

<sup>7</sup>*School of Science, Western Sydney University, Locked Bag 1797, Penrith, NSW 2751, Australia*

### ABSTRACT

The merger shocks generated by the collision of galaxy clusters elevate the pressure within the intracluster medium, significantly influencing the evolution of embedded cluster galaxies. We detect a merger shock (Mach number  $\sim 1.3$ ) on the northwest side of the closest rich galaxy cluster Norma (A3627), using *XMM-Newton* and *Chandra* data. The textbook ram pressure stripping (RPS) galaxy ESO 137-001 appears to be located in the post-shock region. The shock boosts RPS and may induce the formation of the brightest known X-ray tail behind a cluster late-type galaxy. Another prominent head-tail radio galaxy ESO 137-007, with one of the longest radio continuum tails ( $> 500$  kpc), is also likely in the post-shock region. The shock may have reversed the upstream jet to a one-sided radio head-tail morphology. Moreover, the shock can strip and roll the jet cocoon into a vortex ring structure like a ‘smoke ring’ behind the end of the jet as observed by the ASKAP data. Therefore, the cluster merger shock can remarkably change cluster galaxies. Furthermore, Norma is the second brightest non-cool-core cluster following the Coma cluster, with a cool core remnant on its southeast side. Its original cool core may be disrupted by cluster mergers and/or active galactic nuclei.

*Keywords:* Galaxy clusters (584) — Intracluster medium (858) — Shocks (2086) — Tailed radio galaxies (1682) — Ram pressure stripped tails (2126)

### 1. INTRODUCTION

Galaxy clusters form hierarchically through the merger and accretion of smaller substructures at the intersection of the cosmic web. Merging clusters with induced shocks can affect the evolution of cluster member galaxies. The merger shocks increase the pressure of the intracluster medium (ICM), in which member galaxies are embedded. As a result, both star formation and activity in active galactic nuclei (AGNs) can be triggered in gas-rich members as a result of the strong compression of their cold gas by the increased pressure (e.g. K. Bekki et al. 2010; E. Roediger et al. 2014). Boosted AGN and star formation activity have been observed in merging clusters hosting shocks (e.g. K. Umeda et al. 2004; D. Sobral et al. 2015; A. Stroe & D. Sobral 2021).

Moreover, member galaxies moving through the ICM can lose gas via ram pressure stripping (RPS; J. E. Gunn & J. R. Gott 1972; A. Boselli et al. 2022). This stripped gas forms a tail behind the galaxy, and some stripped gas can even turn into stars (e.g. W. J. Cramer et al. 2019; M. Ramatsoku et al. 2019). We call such kinds of galaxies as “RPS galaxies”. The merger shocks can enhance the RPS and star formation in the tails of RPS galaxies, because of the high-pressure shocked ICM (e.g. M. S. Owers et al. 2012; H. Li et al. 2023).

The Norma cluster (A3627; Fig. 1) is the closest massive cluster ( $z = 0.0163$ ,  $M \sim 10^{15} M_{\odot}$ ), and rivals Coma and Perseus in mass and galaxy content (R. C. Kraan-Korteweg et al. 1996). However, it attracts less attention than other nearby luminous clusters due to its proximity to the Galactic plane ( $b \sim -7^{\circ}$ ). A3627 is located at the gravitational center of the Great Attractor and the local Laniakea supercluster, which strongly

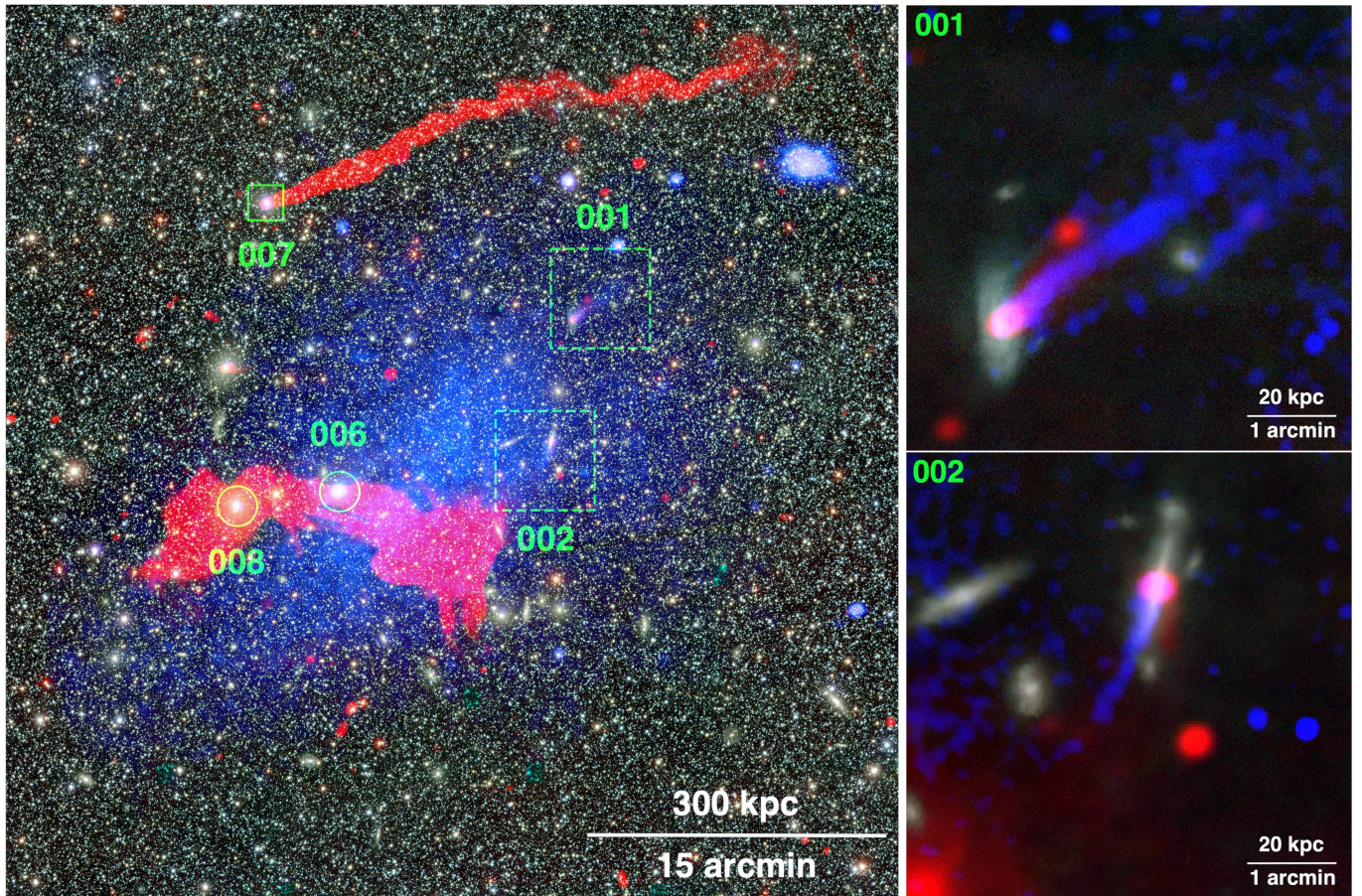


**Figure 1.** *Left:* optical background image from the Dark Energy Camera Legacy Survey (DECaLS; A. Dey et al. 2019) in the  $g, r, z$  bands, overlaid with a red radio image from ASKAP 944 MHz (B. S. Koribalski et al. 2024), and a blue X-ray image from the *XMM-Newton* 0.5-2 keV mosaic. The green circles mark two BCGs, ESO 137-006 and ESO 137-008, the green box marks the head-tail radio galaxy ESO 137-007, and the two green dashed boxes mark two RPS galaxies, ESO 137-001 and ESO 137-002, which are enlarged in the right panels. *Right:* zoom-in images of ESO 137-001 and ESO 137-002, with stars removed from the background DECaLS images using STARNET<sup>a</sup>, overlaid with the red radio image from ASKAP 944 MHz, and the blue X-ray image from the *Chandra* 0.5-2 keV residual image.

<sup>a</sup><https://www.starnetastro.com/>

dominates the growth of the local Universe (e.g. P. A. Woudt et al. 2008; R. B. Tully et al. 2014). A major cluster merger is implied by earlier X-ray observations from the *ROSAT*, *ASCA*, and *Suzaku* that reveal a southeast-northwest (SE-NW) cluster elongation (Fig. 2) and a temperature gradient (5 – 7 keV) in the same direction (H. Boehringer et al. 1996; T. Tamura et al. 1998; S. Nishino et al. 2012). The merger activity is further supported by the large difference in velocity of two brightest cluster galaxies (BCGs; ESO 137-006 at  $\sim 5441$  km s<sup>-1</sup> and ESO 137-008 at  $\sim 3839$  km s<sup>-1</sup>) relative to the mean velocity of the cluster members ( $\sim 4871$  km s<sup>-1</sup>; P. A. Woudt et al. 2008). One of the BCGs, ESO 137-006, is a textbook example of a wide-angle-tail (WAT) radio galaxy (Fig. 1), and is one of the brightest radio galaxies in the southern sky (e.g. P. A. Jones & W. B. McAdam 1996; M. Ramatsoku et al. 2020). Another prominent

radio galaxy is ESO 137-007, which is a head-tail radio galaxy with a tail length of  $> 500$  kpc (Fig. 1), and this is one of the longest radio continuum tails (e.g. P. A. Jones & W. B. McAdam 1996; B. S. Koribalski et al. 2024). A3627 also hosts two spectacular X-ray/H $\alpha$  tails behind RPS galaxies: ESO 137-001 ( $> 80$  kpc; M. Sun et al. 2010) and ESO 137-002 ( $\sim 40$  kpc; M. Sun et al. 2010; B. Zhang et al. 2013). Therefore, A3627 is in the process of an aggressive cluster merger, associated with the formation of a large-scale structure and the violent activity of the member galaxies.

Here we present the discovery of a merger shock on the NW side of A3627. We also report evidence of shock interactions with member galaxies in A3627. Section 2 presents the *Chandra* and *XMM-Newton* data reduction. Section 3 reports the X-ray properties of the cluster and merger shock. Section 4 is the discussion. We present

our conclusions in Section 5. We assume a cosmology with  $H_0 = 70 \text{ km s}^{-1} \text{ Mpc}^{-1}$ ,  $\Omega_m = 0.3$ , and  $\Omega_\Lambda = 0.7$ . At A3627's redshift of  $z = 0.0163$ ,  $1'' = 0.332 \text{ kpc}$ .

## 2. DATA ANALYSIS

We process the *Chandra* and *XMM-Newton* data listed in Table 1, following the procedures of C. Ge et al. (2018). We reduce the *Chandra* ACIS observations with the *Chandra* Interactive Analysis of Observation (CIAO; v4.17) and calibration database (CALDB; v4.12.2), and the *XMM-Newton* EPIC data with the Extended Source Analysis Software (ESAS), as integrated into the *XMM-Newton* Science Analysis System (SAS; v17.0.0). The reduced background-subtracted, exposure-corrected, and smoothed mosaics of A3627 are shown in Fig. 2. The shock detection is mainly attributed to our new deep *XMM-Newton* pointing (obsid = 0920830101).

The spectral analysis is also exclusively performed on the *XMM-Newton* data. We utilize the double-background subtraction method to subtract the instrumental non-X-ray background and X-ray backgrounds separately (C. Ge et al. 2021). Because the X-ray emission in mosaics (Fig. 2) is dominated by A3627, we select an off-cluster region to model the contribution of the X-ray backgrounds. The off-cluster region (obsid = 0601741001 in Table 1, which targets an AGN IGR J16024-6107 with RA = 16:01:47.8, DEC = -61:08:55.2) lies 92 arcmin (1.8 Mpc) away from the A3627 center and is free from diffuse contamination. We use the solar abundance table of M. Asplund et al. (2009) in the spectral fits. We adopt an absorption column density of  $N_{\text{H}} = (2.04 \pm 0.25) \times 10^{21} \text{ cm}^{-2}$  based on the spectral fitting of the X-ray peak (RA = 16:14:16.9, DEC = -60:52:25.9) of A3627. There is a very bright X-ray point source  $\sim 23'$  to the northwest of the cluster peak (Fig. 2), it is a Seyfert 1 galaxy (WKK 6092 with RA = 16:11:51.8, DEC = -60:37:54.9) within the cluster (e.g. H. Boehringer et al. 1996). We also constrain the absorption column density based on the spectral fitting from this Seyfert galaxy of  $N_{\text{H}} = (1.74 \pm 0.17) \times 10^{21} \text{ cm}^{-2}$ , which is consistent with one from the cluster X-ray peak accounting for the errors.

## 3. RESULTS

### 3.1. ICM properties

We first model the global ICM distribution with a  $\beta$ -model (A. Cavaliere & R. Fusco-Femiano 1976). To achieve this, we extract surface brightness profiles (SBPs) centered on the X-ray peak from the *XMM-Newton* image (Fig. 2), excluding regions of point sources and diffuse substructures. Three SBPs are extracted: an azimuthally averaged profile, as well as pro-

**Table 1.** *Chandra* and *XMM-Newton* Observations

ObsID	PI	Date Observed	Exposure (ks) <sup>a</sup>
<i>Chandra</i>			
4956	Jones	2004-06-14	14.5/14.5
4957	Jones	2004-06-14	14.1/14.1
4958	Jones	2004-06-15	14.1/14.1
8178	Sun	2007-07-08	57.4/57.2
9518	Sun	2008-06-13	140.0/139.8
12950	Sun	2011-01-10	89.9/89.5
26789	Nicholl	2023-08-07	50.9/50.7
<i>XMM-Newton</i>			
0208010101	Jones	2004-08-11	16.7(15.0)/12.1(7.8)
0208010201	Jones	2004-08-12	18.5(16.8)/13.1(9.2)
0204250101	Sakelliou	2004-09-19	20.4(16.9)/5.9(2.2)
0550451101	Bassani	2009-02-18	17.6(16.0)/11.8(5.7)
0601741001 <sup>b</sup>	Bassani	2009-09-09	23.6(22.0)/22.6(18.3)
0920830101	Sun/Ge	2024-02-24	89.6(93.6)/84.6(47.9)

<sup>a</sup>: Total/clean exposure time, for *XMM-Newton*, the exposure times are different from MOS and pn (in brackets).

<sup>b</sup>: This is an off-cluster observation to model the X-ray backgrounds.

files along the major and minor axes of A3627. For the major axis profile, we adopt a position angle (PA) of  $126^\circ$  from the north to the east, with opening angles of  $90^\circ$  (the SBP extracted within  $\pm 45^\circ$  of the major axis). The major axis region is excluded for the SBP along the minor axis. We then apply the  $\beta$ -model to fit the SBPs within  $5'$ - $30'$  around the X-ray peak, as there is a central excess of X-ray emission associated with a substructure (H. Boehringer et al. 1996). The  $\beta$ -model gas distribution is given by

$$n_{\text{ICM}}(r) = n_{e0} \left( 1 + \frac{r^2}{r_c^2} \right)^{-\frac{3}{2}\beta}, \quad (1)$$

with the derived X-ray SBP also following a  $\beta$ -model in the form of

$$I_X(r) = I_0 \left( 1 + \frac{r^2}{r_c^2} \right)^{\frac{1}{2}-3\beta}. \quad (2)$$

We apply the analytical formula given by Eq. (3) of C. Ge et al. (2018) to convert the central surface brightness  $I_0$  (from the  $\beta$ -model fitting of the SBP) to the central electron density  $n_{e0}$ . The resulting best-fit parameters are listed below.

Azimuthally averaged :

$$\begin{aligned} n_{e0} &= (2.23 \pm 0.05) \times 10^{-3} \text{ cm}^{-3}, \\ I_0 &= (6.28 \pm 0.09) \times 10^{-6} \text{ counts s}^{-1} \text{ arcsec}^{-2}, \\ r_c &= 629.7 \pm 22.6 \text{ arcsec}, \quad \beta = 0.50 \pm 0.01. \end{aligned}$$

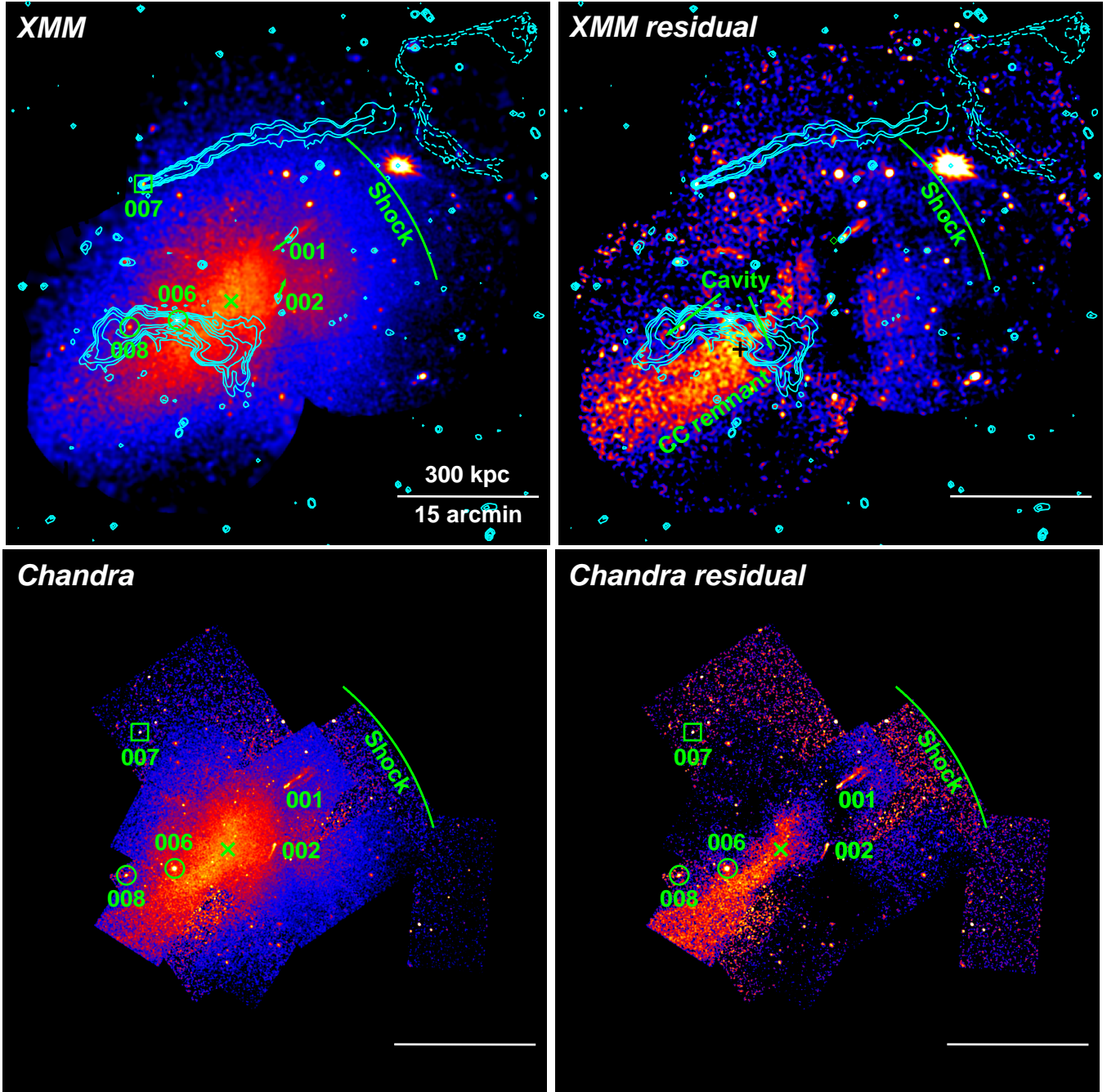


**Figure 2.** *Top left:* *XMM-Newton* 0.5-2 keV mosaic of A3627. The cyan contours are from ASKAP 944 MHz (B. S. Koribalski et al. 2024) and show the WAT radio galaxy ESO 137-006 and the head-tail radio galaxy ESO 137-007 marked by a green box; dashed cyan contours depict the arc-shaped radio filaments resembling a ‘smoke ring’ beyond the radio tail of ESO 137-007. Green circles mark two BCGs: ESO 137-006 and ESO 137-008. The green ‘X’ labels the X-ray peak. Green arrows illustrate the direction of motion of two RPS galaxies with X-ray tails: ESO 137-001 and ESO 137-002. We find a merger shock front (marked by the green arc) indicated by a surface brightness edge on the NW side of the cluster. *Top right:* *XMM-Newton* residual image with the best-fit ICM model subtracted. Prominent residual features include the CC remnant and the X-ray tails of ESO 137-001 or ESO 137-002. The peak of the CC remnant is marked by a black ‘+’. The radio lobes of ESO 137-006 likely excavate two X-ray cavities indicated by the X-ray decrements. *Bottom left:* *Chandra* 0.5-2 keV mosaic marked with bright X-ray sources and tails. *Bottom right:* *Chandra* residual image with the same best-fit ICM model from the *XMM-Newton* image subtracted. The CC remnant with X-ray cavities and the X-ray tails are also remarkable. The same bar at the bottom right of all panels shows 15’/300 kpc.

Along the major axis :

$$\begin{aligned} n_{e0} &= (2.16 \pm 0.05) \times 10^{-3} \text{ cm}^{-3}, \\ I_0 &= (6.59 \pm 0.07) \times 10^{-6} \text{ counts s}^{-1} \text{ arcsec}^{-2}, \\ r_c &= 813.1 \pm 29.0 \text{ arcsec}, \beta = 0.59 \pm 0.02. \end{aligned}$$

Along the minor axis :

$$\begin{aligned} n_{e0} &= (2.25 \pm 0.08) \times 10^{-3} \text{ cm}^{-3}, \\ I_0 &= (5.85 \pm 0.14) \times 10^{-6} \text{ counts s}^{-1} \text{ arcsec}^{-2}, \\ r_c &= 584.5 \pm 33.2 \text{ arcsec}, \beta = 0.51 \pm 0.02. \end{aligned}$$

The density difference at the boundary of major and minor axes is  $\sim 20\%$ , which can be regarded as a systematic error due to the geometry.

The aforementioned  $\beta$ -model fits along the major and minor axes suggest an elliptical surface brightness distribution. To reveal the substructures, we subtract a 2D  $\beta$ -model (`beta2d` in `SHERPA`) from both the *XMM-Newton* and *Chandra* images to produce the residual images in Fig. 2, following procedures given by C. Ge et al. (2020). Notable residual substructures include the bright X-ray tails behind the RPS galaxies ESO 137-001 and ESO 137-002, the SE excess probably from a cool core (CC) remnant, and the NW enhancement from the shock presented in the Sec. 3.2. The SE excess and NW enhancement are also evident in the  $\beta$ -model subtracted residual *ROSAT* image (H. Boehringer et al. 1996).

### 3.2. Merger shock

Early X-ray observations suggest that A3627 is undergoing a major merger event in the SE-NW direction as indicated by the elongated morphology and temperature gradient (H. Boehringer et al. 1996; T. Tamura et al. 1998; S. Nishino et al. 2012). We also produce a temperature map with the Contour Binning algorithm (J. S. Sanders 2006) following C. Ge et al. (2019) in Fig. 3. The *XMM-Newton* and *Chandra* observations confirm the consistent SE-NW morphological elongation and temperature gradient observed in earlier studies. However, they have higher sensitivity and resolution to reveal more details. On the NW side of A3627, we notice a surface brightness edge in Fig. 2, and a temperature drop in the temperature map in Fig. 3. These features are typically produced by a cluster merger shock front (SF). To confirm the presence of this SF and investigate its properties, we extract an SBP and a temperature profile.

The SBP is extracted from the NW of A3627 in self-similar elliptical pie annuli enclosed within the green sector shown in Fig. 3. The shape of the ellipses matches

approximately the sharp outer surface brightness edge. Fig. 3 shows the SBP; the dashed line marks the location of the surface brightness discontinuity with the changes in slope. We fit different power-law functions beside this discontinuity (C. L. Sarazin et al. 2016). The best-fit jump in gas density across the edge is  $\rho_2/\rho_1 = 1.2 \pm 0.1$ , where subscripts 2 and 1 denote the post-shock and pre-shock regions, respectively. We then apply the Rankine-Hugoniot jump conditions (e.g. C. Nolting et al. 2019) to derive the shock Mach number of  $M_p = 1.2 \pm 0.1$ .

Additionally, we measure the temperature jump between the post-shock and pre-shock regions as shown in Fig. 3. The post-shock  $T_X$  is  $6.6 \pm 0.2$  keV, while the pre-shock  $T_X$  is  $6.1 \pm 0.2$  keV. Then we adopt the ‘onion-peeling’ technique (e.g. C. Ge et al. 2019) in elliptical shells to deproject the temperature. The deprojected post-shock  $T_X$  is  $8.2 \pm 0.9$  keV, while the deprojected pre-shock  $T_X$  is  $6.3 \pm 0.7$  keV. The resultant  $T_X$  jump is  $T_2/T_1 = 1.3 \pm 0.2$ . Applying the Rankine-Hugoniot jump condition, we calculate the corresponding Mach number to be  $M_T = 1.3 \pm 0.2$ .

The shock Mach numbers derived from the density and temperature jumps are consistent with each other within the errors. The small discrepancy between the two Mach numbers may be due to the projection effects (e.g. C. Ge et al. 2019). We adopt  $M_i = 1.3$  as the shock Mach number of the ICM in the following discussions.

## 4. DISCUSSION

### 4.1. Shock-bubble interactions

The radio contours in Fig. 2 show two spectacular radio galaxies. One of them is the head-tail radio galaxy ESO 137-007, which has a tail of over 500 kpc with some interesting substructures, including vortex-like features near the position of the SF. Recent 3D MHD simulations suggest that the upstream jet of a radio galaxy may be reversed by the ICM shock, leading to essentially one-sided ‘head-tail’ morphologies of radio galaxies (e.g. T. W. Jones et al. 2017). We note that the green arc in Fig. 2 only denotes part of the large-scale shock surface with a relatively regular shape; the actual large-scale shock front can be more extended and complex as indicated by cluster simulations, and part of the actual shock front may have overrun the radio tails. Although the shock extends beyond the green arc, it does not necessarily have the same curvature as the green arc. An oblique shock wind can also deflect and bend the jet as suggested by simulations, but the two jets may not align with each other (e.g. C. Nolting et al. 2019). The head-tail radio morphology suggests that the shock wind is nearly aligned with the jet.

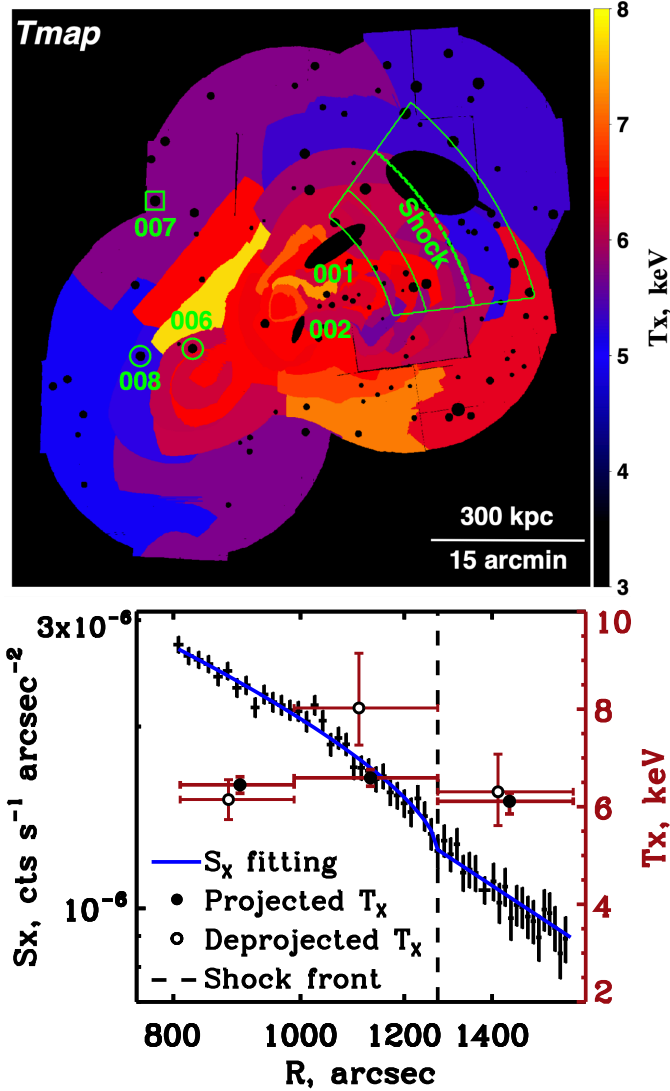


**Figure 3.** *Top:* XMM-Newton temperature map of A3627 with a color bar in units of keV. Regions containing point sources and diffuse substructures are masked as black circles and ellipses. The green sector marks the extraction region for the SBP and the temperature profile shown in the bottom panel. The green dashed line marks the location of the SF. Notable galaxies are marked as in Fig. 2. *Bottom:* SBP and temperature profiles near the shock. The blue solid line shows the best-fit broken power-law model. Black dots are the projected temperature, while open circles are the deprojected temperature. The vertical error bars show  $1\sigma$  uncertainties. The dashed line denotes the location of the SF, where a discontinuity in the density and temperature of the ICM is observed.

The dashed cyan contours in Fig. 2 show the arc-shaped radio filaments extending beyond the radio tail of ESO 137-007. These filaments are likely a partial vortex ring structure generated by the shock. As the shock penetrates the AGN bubble/cocoon/cavity inflated by

the AGN jet, the cocoon is crushed relatively quickly, and the perimeters of the cocoon roll into a vortex ring structure resembling a ‘smoke ring’ (e.g. T. A. Enßlin & M. Brüggen 2002; C. Pfrommer & T. W. Jones 2011; T. W. Jones et al. 2017). Given that the density inside the cocoon is much lower than that in the ICM, the shock velocity is greater inside the cocoon than in the surrounding ICM. Consequently, the internal shock passes through the cocoon much faster than the external shock propagates around it. As the shock passes through the low density cocoon, it indeed moves substantially faster through that region. This significantly distorts the shape of the shock locally, causing it to bulge outward where it passes through the cocoon material. However, the location where the shock is detected will be determined by the large-scale shock surface, which lags behind the region that encountered the cocoon. Therefore, the vortex ring may appear to be on the pre-shock side, despite having passed through the shock. In some circumstances, the cocoon may be crushed and stripped away from the propagating jet before the shock in the external medium propagates around it (e.g. T. W. Jones et al. 2017; C. Nolting et al. 2019). This likely clarifies why the partial vortex ring structure associated with the jet of ESO 137-007 is located behind the external ICM shock in A3627.

Based on the positions of the ICM shock and the radio ring, we can estimate the properties of the cocoon or cavity produced by the AGN jet. From Fig. 2, the external shock is located 450 kpc away from the AGN of ESO 137-007. The internal shock has crushed the cocoon and produced the vortex ring, which is located approximately 760 kpc away from the AGN. The rate of cocoon or cavity collapse is determined by the velocity of the original ICM-cavity contact discontinuity (CD),  $v_{CD}$ . For simplicity and an order-of-magnitude estimation, we can assume that the proper motion of ESO 137-007 is relatively small compared with the shock velocity, and the length of the original jet or cocoon is relatively short compared with that of the current stretched one. Then the velocity ratio between  $v_{CD}$  and the external shock velocity in ICM  $v_{si}$  is  $v_{CD}/v_{si} = 760/450 = 1.7$ . The  $v_{CD}$  obtained in the Riemann solution (e.g. T. W. Jones et al. 2017) is

$$v_{CD} = \frac{2}{\gamma_c + 1} \frac{M_c^2 - 1}{M_c^2} v_{sc}, \quad (3)$$

where  $v_{sc} = M_c a_c$  is the internal shock velocity related to the Mach number  $M_c$  and sound speed  $a_c$  in the cavity. The sound speeds in the ICM and cavity are  $a_i = \sqrt{\gamma_i P_i / \rho_i}$  and  $a_c = \sqrt{\gamma_c P_c / \rho_c}$ , respectively. Assuming the cavity is filled with ultra-hot thermal

plasma ( $\gamma_c = \gamma_i = 5/3$ ) in pressure equilibrium with the ICM ( $P_c = P_i$ ), we have  $a_c/a_i = \sqrt{\rho_i/\rho_c}$  and then  $v_{sc}/v_{si} = (M_c/M_i)\sqrt{\rho_i/\rho_c}$ . Substituting  $v_{sc}$  with  $v_{si}$  in Eq. (3) we get

$$\frac{v_{CD}}{v_{si}} = \frac{2}{\gamma_c + 1} \frac{M_c^2 - 1}{M_c M_i} \sqrt{\frac{\rho_i}{\rho_c}}, \quad (4)$$

then we adopt  $v_{CD}/v_{si} = 1.7$  and  $M_i = 1.3$  to have

$$M_c - \frac{1}{M_c} = 2.9\sqrt{\delta}, \quad (5)$$

where  $\delta = \rho_c/\rho_i$  is the density contrast between the cavity and ICM. For a typical density contrast of  $\delta = 0.001 - 0.01$  (e.g. C. Pfrommer & T. W. Jones 2011; C. Nolting et al. 2019), the Mach number in the cavity is  $M_c = 1.05 - 1.16$ , which is also a weak shock. Moreover, the resultant  $M_c$  is insensitive to the velocity ratio  $v_{CD}/v_{si}$ . Therefore, even if the proper motion of ESO 137-007 and the length of the original jet cannot be ignored, although the velocity ratio  $v_{CD}/v_{si}$  changes, the results remain largely unchanged. However, in the weak shock limit,  $v_{sc}/v_{si} \sim 1/\sqrt{\delta}$  (e.g. T. W. Jones et al. 2017), the internal shock velocity in the cavity is much larger than the external shock velocity in the ICM due to the extreme density contrast. This substantial velocity difference represents a large velocity shear at the boundary between the cavity and the external medium, and this shear leads to the generation of vorticity and the vortex ring. In the case of ESO 137-007 in A3627, the pre-shock average temperature is  $T_X \sim 6$  keV, the corresponding ICM sound speed is  $a_i = \sqrt{\frac{\gamma k T}{\mu m_p}} = 1264$  km s<sup>-1</sup>. Then the related external shock speed is  $v_{si} = 1643$  km s<sup>-1</sup>, the cavity collapse velocity is  $v_{CD} = 2793$  km s<sup>-1</sup>, and the internal shock velocity is  $v_{sc} \gtrsim 16430$  km s<sup>-1</sup>. The cavity collapse velocity  $v_{CD}$  is between the external shock velocity  $v_{si}$  and the internal shock velocity  $v_{sc}$ . Therefore, the cavity is crushed before the ICM shock propagates around it, as observed.

Later, after the vortex ring has been advected away, a naked jet without a cocoon remains, like the ‘‘source C’’ in A2256 (e.g. T. W. Jones et al. 2017; C. Nolting et al. 2019). We also detect a merger shock near the end of the jet of ‘‘source C’’ in A2256 (C. Ge et al. 2020), which indicates that the jet plasma cocoon has been stripped away by the shock.

The shock-bubble interactions may also explain the origin of the odd radio circles (ORCs), which are circles of radio continuum emission with low surface brightness (e.g. R. P. Norris et al. 2021; B. S. Koribalski et al. 2021). The shock impact can turn the jet cocoons or lobes into vortex ring structures (e.g. C. Nolting et al.

2019). If our line of sight is near the jet or lobe axis, the vortex ring structures may resemble the ORC. Simulations suggest that shock reacceleration of remnant radio lobes can lead to ORC-like radio morphologies (e.g. S. S. Shabala et al. 2024).

#### 4.2. Shocks enhance RPS

Similar to the way an explosive shock wave strips leaves from trees, the cluster merger shock can remove gas from member galaxies. Simulations suggest that large-scale strong shocks can significantly enhance RPS. These shocks can accelerate the ICM gas and increase its density, thereby boosting ram pressure. In some extreme cases, the ram pressure can surge by 1–3 orders of magnitude (e.g. H. Li et al. 2023). The signatures of RPS are notably prevalent in merging clusters that host potential merger shocks (e.g. A. Stroe et al. 2015; R. Ruggiero et al. 2019; H. Ebeling & B. S. Kalita 2019). In particular, RPS galaxies tend to be found near cluster merger shocks (e.g. M. S. Owers et al. 2012; C. Ge et al. 2019).

The RPS galaxy ESO 137-001 is potentially in the post-shock region as indicated by the higher temperature in the temperature map (Fig. 3), while the RPS galaxy ESO 137-002 is at a greater projected distance from the SF. The shock may have overrun ESO 137-001, thereby enhancing the ambient ICM pressure and thus promoting the tail formation and star forming in tails (e.g. E. Roediger et al. 2014). Although the star formation rates ( $\sim 1 M_\odot$  yr<sup>-1</sup>) in ESO 137-001 and ESO 137-002 are comparable, star formation is notably more active in the tails of ESO 137-001 than in those of ESO 137-002 (e.g. S. Laudari et al. 2022; W. Waldron et al. 2023). As shown in Fig. 1, the X-ray tails ( $> 80$  kpc) of ESO 137-001 are also longer and brighter than those ( $\sim 40$  kpc) of ESO 137-002 (e.g. M. Sun et al. 2010; B. Zhang et al. 2013). Additionally, the geometry of mergers involving shocks and bright RPS galaxies is similar between A3627 (e.g. RPS galaxy ESO 137-001; M. Sun et al. 2006, 2010) and A1367 (e.g. RPS galaxy UGC 6697; M. Sun & A. Vikhlinin 2005; C. Ge et al. 2019).

If we assume that ESO 137-001 is falling into A3627 in the plane of the sky with a velocity of  $\sim 1000$  km s<sup>-1</sup>, and the shock of A3627 has swept through it. We can then estimate the enhancement of ram pressure due to the shock with the standard Rankine–Hugoniot relations (e.g. C. Nolting et al. 2019). We also adopt an ICM shock Mach number  $M_i = 1.3$ , then the density ratio is  $\rho_w/\rho_i = 1.4$ , where  $\rho_w$  is the density in the post-shock wind and  $\rho_i$  is the density in the pre-shock ICM. The post-shock wind velocity (e.g. T. W. Jones et al. 2017)

is

$$v_w = \frac{3 M_i^2 - 1}{4 M_i} a_i, \quad (6)$$

and  $a_i = 1264 \text{ km s}^{-1}$  is the sound speed of the ICM in A3627. Then the wind velocity induced by the shock is  $v_w = 503 \text{ km s}^{-1}$ . Because the wind velocity is in the opposite direction to the galaxy velocity  $v_g$ , the galaxy velocity relative to the ICM in the post-shock wind is  $v_{gw} = 1503 \text{ km s}^{-1}$ . The ratio of ram pressure after and before the shock is  $\frac{\rho_w}{\rho_i} \left(\frac{v_{gw}}{v_g}\right)^2 = 1.4 \times 1.5^2 = 3.2$ . Even a weak shock can enhance the ram pressure significantly. Furthermore, the shock Mach numbers derived from the X-ray observations are typically underestimated due to, e.g., the projection effects (e.g. H. Akamatsu et al. 2017; C. Zhang et al. 2019). Simulations of cluster formation show that shocks are actually rather complex and inhomogeneous, and that the shock strengths vary with location. The galaxy may have encountered a shock with a larger Mach number. If the actual shock near ESO 137-001 has a moderate Mach number of  $M_i \sim 2$ , the ram pressure can be boosted by a factor of 13. Therefore, the formation of the brightest known X-ray tail behind the cluster late-type galaxy ESO 137-001 may be attributed to the shock.

Fig. 1 also illustrates radio tails from the synchrotron radiation produced by relativistic electrons moving within magnetic fields behind these RPS galaxies (e.g. B. S. Koribalski et al. 2024). The radio tail of ESO 137-001 is spatially correlated with its X-ray tail, suggesting that most relativistic electrons originate from the host galaxy plasma stripped away by the ram pressure. The radio tail is shorter than the X-ray tail, because its length is limited by the radiative synchrotron and inverse-Compton cooling (e.g. H. Chen et al. 2020). The radio tail of ESO 137-002 is offset  $\sim 30^\circ$  from its X-ray tail. Unlike ESO 137-001, which is a star-forming galaxy (e.g. M. Fossati et al. 2016), ESO 137-002 hosts a Seyfert2-like AGN (e.g. M. Sun et al. 2010). The radio tail of ESO 137-002 likely represents a nuclear jet that has been deflected or bent by the ram pressure of the wind (e.g. C. Nolting et al. 2019).

#### 4.3. Cause of the cool core remnant

The global morphology of A3627 is significantly disturbed by the cluster merger, leading to an extension and distortion of its central core region. We estimate the cooling time of the central region using an electron density  $n_{e0} = 2.23 \times 10^{-3} \text{ cm}^{-3}$  derived from the  $\beta$ -model fitting, along with a temperature  $T_X = 6.4 \text{ keV}$  and metallicity  $Z = 0.55 Z_\odot$  obtained from the spectral fitting of a circular region (radius  $\sim 3'$ ) around the X-ray peak with the APEC model. The calculated central

cooling time is approximately 21.5 Gyr, determined by dividing the total thermal energy by the X-ray emissivity, expressed as  $(3/2)n_{\text{tot}}kT/(n_e n_H \Lambda)$  where the total particle density  $n_{\text{tot}} = 1.93n_e$ , and  $\Lambda$  is the cooling rate calculated from the APEC model in XSPEC (K. A. Arnaud 1996), in the 0.01 - 100 keV band. Meanwhile, the computed central entropy  $kT/n_e^{2/3}$  is  $375 \text{ keV cm}^2$ . Thus, A3627 is a typical non-CC cluster according to the criteria of, e.g. D. S. Hudson et al. (2010). In fact, it is the second brightest non-CC cluster following the Coma cluster (H. Boehringer et al. 1996). Residual *XMM-Newton* and *Chandra* images in Fig. 2 show an SE excess, likely associated with a CC remnant as the remains of a CC after a heating event (e.g. M. Rossetti & S. Molendi 2010). To search for the metal abundance excess that may be linked to this CC remnant, we extract spectra and estimate the metallicities from circular regions (radius  $\sim 3'$ ) centered on the X-ray peak (the 'X' region in Fig. 2, yielding  $0.55 \pm 0.12 Z_\odot$ ) and on the remnant peak (the '+' region in Fig. 2, yielding  $0.53 \pm 0.10 Z_\odot$ ). These values are then compared with the metallicity derived from a surrounding annular region (radii  $\sim 8'$ - $11'$  around both the X-ray peak and the remnant peak), which gives  $0.34 \pm 0.05 Z_\odot$ . The significant metallicity excess supports the notion that the SE excess feature is a CC remnant (e.g. M. Rossetti & S. Molendi 2010).

Observations find that cluster core properties correlate with the dynamical state or ICM morphology: CC clusters tend to be dynamically relaxed with regular morphology, while non-CC clusters are often dynamically young with disturbed morphology (e.g. Y. Chen et al. 2007; G. W. Pratt et al. 2010; Z. S. Yuan et al. 2022). Simulations indicate that CCs can be disrupted by cluster mergers and heated through shock-heating and mixing (e.g. J. A. ZuHone 2011; R. Valdarnini & C. L. Sarazin 2021). Thus, the significant merger event in A3627 may have disrupted and heated its original CC to a CC remnant.

However, cluster mergers are not the sole cause of CC remnants, as indicated by simulations (e.g. E. Rasia et al. 2015; D. J. Barnes et al. 2018). AGNs can also heat and perturb CCs (e.g. S. Ehlert et al. 2011; W. Liu et al. 2024). Occasionally, large CC clusters experience strong AGN outbursts. During such events, powerful radio jets penetrate the inner regions of CCs, depositing substantial energy into the outer regions. The CC can be disrupted and turned into a CC remnant or corona. If the CC is completely destroyed, a non-CC may form (e.g. M. Sun 2009; W. Liu et al. 2024). In particular, in A3627, its BCG ESO 137-006 embeds one of the brightest coronae in clusters (M. Sun 2009). ESO 137-006 also hosts the WAT source PKS 1610-60, as one of the

brightest radio sources (P. A. Jones & W. B. McAdam 1996). The radio lobes of PKS 1610-60 excavate the X-ray cavities in Fig. 2, providing compelling evidence of AGN feedback and CC disruption.

The total energy required to excavate a cavity is equal to its enthalpy, given by

$$E_{cav} = \frac{\gamma}{\gamma - 1} pV, \quad (7)$$

where  $p$  is the pressure of the gas surrounding the cavity,  $V$  is the cavity's volume, and  $\gamma$  is the ratio of specific heats of the cavity plasma;  $\gamma = 4/3$  for relativistic plasma and  $\gamma = 5/3$  for nonrelativistic plasma (e.g. B. R. McNamara & P. E. J. Nulsen 2007). For the cavities of PKS 1610-60 filled with radio lobes, we adopt  $\gamma = 4/3$ , and the enthalpy is  $4pV$ . For an order-of-magnitude estimation, we assume the cavity is spherical and find its radius to be  $\sim 45$  kpc. The thermal pressure of the surrounding ICM,  $p = n_{tot}kT$ , is derived with  $n_{tot}$  from the best-fit  $\beta$ -model and  $T$  from the temperature map. Then the AGN feedback energy traced by the cavities is  $E_{cav} = 2.6 \times 10^{60}$  erg. The age of the cavity is calculated as the time required for the cavity to rise the projected distance ( $R \sim 127$  kpc) from the radio core to its present location at the speed of sound,  $t_{cav} = R/a_i = 9.8 \times 10^7$  yr (e.g. L. Birzan et al. 2004). The cavity power is  $P_{cav} = E_{cav}/t_{cav} = 8.3 \times 10^{44}$  ergs  $s^{-1}$ , which represents a lower limit to the total power of the AGN, because the remaining roughly half of the AGN feedback energy is deposited into the ICM through the shock (e.g. B. R. McNamara & P. E. J. Nulsen 2007). This amount of feedback energy deposited into the ICM can heat the central gas within  $\sim 100$  kpc (a typical cooling radius of clusters; e.g. L. Birzan et al. 2004; D. A. Rafferty et al. 2006). In the central region, the cooling through X-ray emission is  $L_X = \int n_e n_H \Lambda dV = 9.2 \times 10^{42}$  ergs  $s^{-1}$ , where the densities are from the best-fit  $\beta$ -model and the  $\Lambda$  is the cooling rate calculated from the APEC model in XSPEC in the 0.01 - 100 keV band. Compared with the cavity power, the cooling can be ignored. The total number of particles in the central region is  $N = \int n_{tot} dV = 4.8 \times 10^{68}$ , and they can be heated with  $E_{cav} \sim (3/2)Nk\Delta T$ . Thus, the increase in central temperature is  $k\Delta T \sim 2.3$  keV per particle, which can significantly heat the central re-

gion and potentially smear out the temperature difference between the CC and the surrounding gas. Furthermore, hydrodynamical simulations show that AGN feedback and cluster mergers work together to increase the central entropy and destroy the CCs (e.g. S.-S. Chen et al. 2024; K. Lehle et al. 2025).

## 5. CONCLUSIONS

We revisit the closest rich cluster, A3627, with *XMM-Newton* and *Chandra* mosaic. After subtracting the global 2D  $\beta$ -model of the ICM, two prominent substructures are identified: an enhancement in the NW and an excess in the SE.

The NW enhancement is related to a merger shock identified from the jumps in ICM density and temperature. The merger shock substantially elevates the ICM pressure and induces shocking features in the cluster galaxies. Two extreme cases are the RPS galaxy ESO 137-001 and the head-tail radio galaxy ESO 137-007. The shock is likely to have overrun ESO 137-001, promoting the tail formation and star forming in its tail. For ESO 137-007, the shock may reverse its upstream jet to a one-sided radio head-tail morphology, strip and roll the jet cocoon into a vortex ring behind the jet.

The SE excess is a CC remnant. The original CC has probably been destroyed by the violent cluster merger, and/or by the AGN feedback from ESO 137-006, which is one of the brightest radio sources.

In summary, the interactions between the ICM and member galaxies significantly influence the evolution of both. A3627 provides an ideal laboratory for investigating these interactions.

## ACKNOWLEDGMENTS

We thank the anonymous referee for the helpful suggestions. This research has made use of data and/or software provided by the High Energy Astrophysics Science Archive Research Center (HEASARC). C.G. acknowledges support from the National Natural Science Foundation of China (Nos. 12373007, 12422302).

This research employs a list of Chandra datasets, obtained by the Chandra X-ray Observatory, contained in DOI: 10.25574/cdc.526.

## REFERENCES

- Akamatsu, H., Mizuno, M., Ota, N., et al. 2017, *A&A*, 600, A100, doi: 10.1051/0004-6361/201628400
- Arnaud, K. A. 1996, in *Astronomical Society of the Pacific Conference Series*, Vol. 101, *Astronomical Data Analysis Software and Systems V*, ed. G. H. Jacoby & J. Barnes, 17

- Asplund, M., Grevesse, N., Sauval, A. J., & Scott, P. 2009, *ARA&A*, 47, 481, doi: [10.1146/annurev.astro.46.060407.145222](https://doi.org/10.1146/annurev.astro.46.060407.145222)
- Barnes, D. J., Vogelsberger, M., Kannan, R., et al. 2018, *MNRAS*, 481, 1809, doi: [10.1093/mnras/sty2078](https://doi.org/10.1093/mnras/sty2078)
- Bekki, K., Owers, M. S., & Couch, W. J. 2010, *ApJL*, 718, L27, doi: [10.1088/2041-8205/718/1/L27](https://doi.org/10.1088/2041-8205/718/1/L27)
- Birzan, L., Rafferty, D. A., McNamara, B. R., Wise, M. W., & Nulsen, P. E. J. 2004, *ApJ*, 607, 800, doi: [10.1086/383519](https://doi.org/10.1086/383519)
- Boehringer, H., Neumann, D. M., Schindler, S., & Kraan-Korteweg, R. C. 1996, *ApJ*, 467, 168, doi: [10.1086/177592](https://doi.org/10.1086/177592)
- Boselli, A., Fossati, M., & Sun, M. 2022, *A&A Rv*, 30, 3, doi: [10.1007/s00159-022-00140-3](https://doi.org/10.1007/s00159-022-00140-3)
- Cavaliere, A., & Fusco-Femiano, R. 1976, *A&A*, 500, 95
- Chen, H., Sun, M., Yagi, M., et al. 2020, *MNRAS*, 496, 4654, doi: [10.1093/mnras/staa1868](https://doi.org/10.1093/mnras/staa1868)
- Chen, S.-S., Yang, H.-Y. K., Schive, H.-Y., ZuHone, J., & Gaspari, M. 2024, arXiv e-prints, arXiv:2412.13595, doi: [10.48550/arXiv.2412.13595](https://doi.org/10.48550/arXiv.2412.13595)
- Chen, Y., Reiprich, T. H., Böhringer, H., Ikebe, Y., & Zhang, Y. Y. 2007, *A&A*, 466, 805, doi: [10.1051/0004-6361:20066471](https://doi.org/10.1051/0004-6361:20066471)
- Cramer, W. J., Kenney, J. D. P., Sun, M., et al. 2019, *ApJ*, 870, 63, doi: [10.3847/1538-4357/aaefff](https://doi.org/10.3847/1538-4357/aaefff)
- Dey, A., Schlegel, D. J., Lang, D., et al. 2019, *AJ*, 157, 168, doi: [10.3847/1538-3881/ab089d](https://doi.org/10.3847/1538-3881/ab089d)
- Ebeling, H., & Kalita, B. S. 2019, *ApJ*, 882, 127, doi: [10.3847/1538-4357/ab35d6](https://doi.org/10.3847/1538-4357/ab35d6)
- Ehlert, S., Allen, S. W., von der Linden, A., et al. 2011, *MNRAS*, 411, 1641, doi: [10.1111/j.1365-2966.2010.17801.x](https://doi.org/10.1111/j.1365-2966.2010.17801.x)
- Enßlin, T. A., & Brüggen, M. 2002, *MNRAS*, 331, 1011, doi: [10.1046/j.1365-8711.2002.05261.x](https://doi.org/10.1046/j.1365-8711.2002.05261.x)
- Fossati, M., Fumagalli, M., Boselli, A., et al. 2016, *MNRAS*, 455, 2028, doi: [10.1093/mnras/stv2400](https://doi.org/10.1093/mnras/stv2400)
- Ge, C., Wang, Q. D., Burchett, J. N., et al. 2018, *MNRAS*, 481, 4111, doi: [10.1093/mnras/sty2492](https://doi.org/10.1093/mnras/sty2492)
- Ge, C., Sun, M., Liu, R.-Y., et al. 2019, *MNRAS*, 486, L36, doi: [10.1093/mnrasl/slz049](https://doi.org/10.1093/mnrasl/slz049)
- Ge, C., Liu, R.-Y., Sun, M., et al. 2020, *MNRAS*, 497, 4704, doi: [10.1093/mnras/staa2320](https://doi.org/10.1093/mnras/staa2320)
- Ge, C., Sun, M., Yagi, M., et al. 2021, *MNRAS*, 508, L69, doi: [10.1093/mnrasl/slab108](https://doi.org/10.1093/mnrasl/slab108)
- Gunn, J. E., & Gott, III, J. R. 1972, *ApJ*, 176, 1, doi: [10.1086/151605](https://doi.org/10.1086/151605)
- Hudson, D. S., Mittal, R., Reiprich, T. H., et al. 2010, *A&A*, 513, A37, doi: [10.1051/0004-6361/200912377](https://doi.org/10.1051/0004-6361/200912377)
- Jones, P. A., & McAdam, W. B. 1996, *MNRAS*, 282, 137, doi: [10.1093/mnras/282.1.137](https://doi.org/10.1093/mnras/282.1.137)
- Jones, T. W., Nolting, C., O'Neill, B. J., & Mendygral, P. J. 2017, *Physics of Plasmas*, 24, 041402, doi: [10.1063/1.4978620](https://doi.org/10.1063/1.4978620)
- Koribalski, B. S., Norris, R. P., Andernach, H., et al. 2021, *MNRAS*, 505, L11, doi: [10.1093/mnrasl/slab041](https://doi.org/10.1093/mnrasl/slab041)
- Koribalski, B. S., Duchesne, S. W., Lenc, E., et al. 2024, *MNRAS*, 533, 608, doi: [10.1093/mnras/stae1838](https://doi.org/10.1093/mnras/stae1838)
- Kraan-Korteweg, R. C., Woudt, P. A., Cayatte, V., et al. 1996, *Nature*, 379, 519, doi: [10.1038/379519a0](https://doi.org/10.1038/379519a0)
- Laudari, S., Jáchym, P., Sun, M., et al. 2022, *MNRAS*, 509, 3938, doi: [10.1093/mnras/stab3280](https://doi.org/10.1093/mnras/stab3280)
- Lehle, K., Nelson, D., & Pillepich, A. 2025, *A&A*, 702, A25, doi: [10.1051/0004-6361/202554374](https://doi.org/10.1051/0004-6361/202554374)
- Li, H., Wang, H., Mo, H. J., et al. 2023, *ApJ*, 942, 44, doi: [10.3847/1538-4357/aca7bd](https://doi.org/10.3847/1538-4357/aca7bd)
- Liu, W., Sun, M., Voit, G. M., et al. 2024, *MNRAS*, 531, 2063, doi: [10.1093/mnras/stae1285](https://doi.org/10.1093/mnras/stae1285)
- McNamara, B. R., & Nulsen, P. E. J. 2007, *ARA&A*, 45, 117, doi: [10.1146/annurev.astro.45.051806.110625](https://doi.org/10.1146/annurev.astro.45.051806.110625)
- Nishino, S., Fukazawa, Y., & Hayashi, K. 2012, *PASJ*, 64, 16, doi: [10.1093/pasj/64.1.16](https://doi.org/10.1093/pasj/64.1.16)
- Nolting, C., Jones, T. W., O'Neill, B. J., & Mendygral, P. J. 2019, *ApJ*, 876, 154, doi: [10.3847/1538-4357/ab16d6](https://doi.org/10.3847/1538-4357/ab16d6)
- Norris, R. P., Intema, H. T., Kapińska, A. D., et al. 2021, *PASA*, 38, e003, doi: [10.1017/pasa.2020.52](https://doi.org/10.1017/pasa.2020.52)
- Owers, M. S., Couch, W. J., Nulsen, P. E. J., & Randall, S. W. 2012, *ApJL*, 750, L23, doi: [10.1088/2041-8205/750/1/L23](https://doi.org/10.1088/2041-8205/750/1/L23)
- Pfrommer, C., & Jones, T. W. 2011, *ApJ*, 730, 22, doi: [10.1088/0004-637X/730/1/22](https://doi.org/10.1088/0004-637X/730/1/22)
- Pratt, G. W., Arnaud, M., Piffaretti, R., et al. 2010, *A&A*, 511, A85, doi: [10.1051/0004-6361/200913309](https://doi.org/10.1051/0004-6361/200913309)
- Rafferty, D. A., McNamara, B. R., Nulsen, P. E. J., & Wise, M. W. 2006, *ApJ*, 652, 216, doi: [10.1086/507672](https://doi.org/10.1086/507672)
- Ramatsoku, M., Serra, P., Poggianti, B. M., et al. 2019, *MNRAS*, 487, 4580, doi: [10.1093/mnras/stz1609](https://doi.org/10.1093/mnras/stz1609)
- Ramatsoku, M., Murgia, M., Vacca, V., et al. 2020, *A&A*, 636, L1, doi: [10.1051/0004-6361/202037800](https://doi.org/10.1051/0004-6361/202037800)
- Rasia, E., Borgani, S., Murante, G., et al. 2015, *ApJL*, 813, L17, doi: [10.1088/2041-8205/813/1/L17](https://doi.org/10.1088/2041-8205/813/1/L17)
- Roediger, E., Brüggen, M., Owers, M. S., Ebeling, H., & Sun, M. 2014, *MNRAS*, 443, L114, doi: [10.1093/mnrasl/slu087](https://doi.org/10.1093/mnrasl/slu087)
- Rossetti, M., & Molendi, S. 2010, *A&A*, 510, A83, doi: [10.1051/0004-6361/200913156](https://doi.org/10.1051/0004-6361/200913156)
- Ruggiero, R., Machado, R. E. G., Roman-Oliveira, F. V., et al. 2019, *MNRAS*, 484, 906, doi: [10.1093/mnras/sty3422](https://doi.org/10.1093/mnras/sty3422)

- Sanders, J. S. 2006, MNRAS, 371, 829,  
doi: [10.1111/j.1365-2966.2006.10716.x](https://doi.org/10.1111/j.1365-2966.2006.10716.x)
- Sarazin, C. L., Finoguenov, A., Wik, D. R., & Clarke, T. E. 2016, arXiv e-prints, arXiv:1606.07433,  
doi: [10.48550/arXiv.1606.07433](https://doi.org/10.48550/arXiv.1606.07433)
- Shabala, S. S., Yates-Jones, P. M., Jerrim, L. A., et al. 2024, PASA, 41, e024, doi: [10.1017/pasa.2024.11](https://doi.org/10.1017/pasa.2024.11)
- Sobral, D., Stroe, A., Dawson, W. A., et al. 2015, MNRAS, 450, 630, doi: [10.1093/mnras/stv521](https://doi.org/10.1093/mnras/stv521)
- Stroe, A., & Sobral, D. 2021, ApJ, 912, 55,  
doi: [10.3847/1538-4357/abe7f8](https://doi.org/10.3847/1538-4357/abe7f8)
- Stroe, A., Sobral, D., Dawson, W., et al. 2015, MNRAS, 450, 646, doi: [10.1093/mnras/stu2519](https://doi.org/10.1093/mnras/stu2519)
- Sun, M. 2009, ApJ, 704, 1586,  
doi: [10.1088/0004-637X/704/2/1586](https://doi.org/10.1088/0004-637X/704/2/1586)
- Sun, M., Donahue, M., Roediger, E., et al. 2010, ApJ, 708, 946, doi: [10.1088/0004-637X/708/2/946](https://doi.org/10.1088/0004-637X/708/2/946)
- Sun, M., Jones, C., Forman, W., et al. 2006, ApJL, 637, L81, doi: [10.1086/500590](https://doi.org/10.1086/500590)
- Sun, M., & Vikhlinin, A. 2005, ApJ, 621, 718,  
doi: [10.1086/427728](https://doi.org/10.1086/427728)
- Tamura, T., Fukazawa, Y., Kaneda, H., et al. 1998, PASJ, 50, 195, doi: [10.1093/pasj/50.2.195](https://doi.org/10.1093/pasj/50.2.195)
- Tully, R. B., Courtois, H., Hoffman, Y., & Pomarède, D. 2014, Nature, 513, 71, doi: [10.1038/nature13674](https://doi.org/10.1038/nature13674)
- Umeda, K., Yagi, M., Yamada, S. F., et al. 2004, ApJ, 601, 805, doi: [10.1086/380555](https://doi.org/10.1086/380555)
- Valdarnini, R., & Sarazin, C. L. 2021, MNRAS, 504, 5409,  
doi: [10.1093/mnras/stab1126](https://doi.org/10.1093/mnras/stab1126)
- Waldron, W., Sun, M., Luo, R., et al. 2023, MNRAS, 522, 173, doi: [10.1093/mnras/stad963](https://doi.org/10.1093/mnras/stad963)
- Woudt, P. A., Kraan-Korteweg, R. C., Lucey, J., Fairall, A. P., & Moore, S. A. W. 2008, MNRAS, 383, 445,  
doi: [10.1111/j.1365-2966.2007.12571.x](https://doi.org/10.1111/j.1365-2966.2007.12571.x)
- Yuan, Z. S., Han, J. L., & Wen, Z. L. 2022, MNRAS, 513, 3013, doi: [10.1093/mnras/stac1037](https://doi.org/10.1093/mnras/stac1037)
- Zhang, B., Sun, M., Ji, L., et al. 2013, ApJ, 777, 122,  
doi: [10.1088/0004-637X/777/2/122](https://doi.org/10.1088/0004-637X/777/2/122)
- Zhang, C., Churazov, E., Forman, W. R., & Jones, C. 2019, MNRAS, 482, 20, doi: [10.1093/mnras/sty2501](https://doi.org/10.1093/mnras/sty2501)
- ZuHone, J. A. 2011, ApJ, 728, 54,  
doi: [10.1088/0004-637X/728/1/54](https://doi.org/10.1088/0004-637X/728/1/54)